

Electron-doping dependence of the anisotropic superconductivity in $\text{BaFe}_{2-x}\text{Ni}_x\text{As}_2$

Zhaosheng Wang,^{1,*} Tao Xie,² E. Kampert,¹ T. Förster,¹ Xingye Lu,² Rui Zhang,²
Dongliang Gong,² Shiliang Li,^{2,3} T. Herrmannsdörfer,¹ J. Wosnitza,¹ and Huiqian Luo^{2,†}

¹*Hochfeld-Magnetlabor Dresden (HLD-EMFL), Helmholtz-Zentrum Dresden-Rossendorf, D-01314 Dresden, Germany*

²*Beijing National Laboratory for Condensed Matter Physics,*

Institute of Physics, Chinese Academy of Sciences, Beijing 100190, China

³*Collaborative Innovation Center of Quantum Matter, Beijing, China*

The upper critical field (H_{c2}) in superconducting $\text{BaFe}_{2-x}\text{Ni}_x\text{As}_2$ single crystals has been determined by magnetotransport measurements down to 0.6 K over the whole superconducting dome with $0.065 \leq x \leq 0.22$, both for the inter-plane ($H \parallel c$, H_{c2}^c) and in-plane ($H \parallel ab$, H_{c2}^{ab}) field directions in static magnetic fields up to 16 T and pulsed magnetic fields up to 60 T. The temperature dependence of H_{c2}^{ab} follows the Werthamer-Helfand-Hohenberg (WHH) model incorporating orbital and spin paramagnetic effects, while $H_{c2}^c(T)$ can only be described by the effective two-band model with unbalanced diffusivity. The anisotropy of the upper critical fields, $\gamma(T) = H_{c2}^{ab}/H_{c2}^c$ monotonically increases with increasing temperature for all dopings, and its zero-temperature limit, $\gamma(0)$, has an asymmetric doping dependence with a significant enhancement in the overdoped regime, where the optimally doped compound has the most isotropic superconductivity. Our results suggest that the anisotropy in the superconductivity of iron pnictides is determined by the topology of the Fermi surfaces together with the doping-induced impurity scattering.

PACS numbers: 74.25.F-, 74.25.Op, 74.70.-b

I. INTRODUCTION

Determining the upper critical field (H_{c2}), where superconductivity ceases in a type-II superconductor, is one of the most important steps for gathering an understanding of unconventional superconductivity including the pairing mechanism, the pairing strength, as well as the coherence length. Particularly, the temperature dependence of H_{c2} reflects the underlying electronic structure responsible for superconductivity and provides valuable information on the microscopic origin of pair breaking, which is important for various application purposes, too. Most iron-based superconductors have a moderate H_{c2} , within the range of non-destructive pulsed high magnetic fields available in current technology¹⁻¹⁰. This makes it possible to obtain H_{c2} and its anisotropy $\gamma = H_{c2}^{ab}/H_{c2}^c$ down to the zero-temperature limit experimentally, rather than by use of imprecise theoretical extrapolations from data near the superconducting transition temperature (T_c) only. Although all iron-based superconductors have a layered structure. The 122 and 111 families always show a nearly isotropic $H_{c2}(0)$ at zero temperature [$\gamma(0) \approx 1$]⁶⁻⁹, and the 111 family has a slightly higher $\gamma(0) \approx 1.5$ ^{10,11}, while the anisotropy of $H_{c2}(0)$ for the 1111 family with the highest T_c is not well determined yet due to the very high H_{c2} (above 100 T)³⁻⁵. Moreover, it should be noticed that, until now most results are from optimally doped compounds or intrinsically superconducting samples and reports on the doping dependence of H_{c2} and γ at low temperature in iron pnictides are scarce.

BaFe_2As_2 (Ba-122), as a parent phase of the iron-based superconductors with a double-layered structure, can be doped either with holes by replacing Ba with K/Na or with electrons by substituting Fe with Ni/Co to suppress antiferromagnetism (AFM) and induce superconductivity¹²⁻¹⁷. Specifically in the $\text{BaFe}_{2-x}\text{Ni}_x\text{As}_2$ system, upon doping electrons by Ni substitution, the Néel temperature (T_N) and orthorhombic lattice distortion temperature (T_s) are gradually suppressed and vanish

at about $x = 0.11$. Superconductivity emerges at $x = 0.05$, then reaches the maximum critical temperature (T_c) at about 20 K around $x = 0.1$, and finally disappears in the overdoped regime at $x = 0.25$ [Fig. 1(a)]^{18,19}. Based on a rigid-band model, the doped electrons simply shift the chemical potential, which shrinks the hole pocket at the Γ point and enlarges the electron pocket at the M point, respectively [Fig. 1(b)]²⁰. Although the real case is more complicated due to additional effects from impurities^{21,22}, the experimental results qualitatively agree with the rigid-band model²³. Moreover, all Fermi-surface sheets show warping along the k_z direction, and the hole sheet becomes more three-dimensional (3D) upon electron doping into the overdoped regime²⁴. Thus, a more isotropic superconductivity corresponding to the 3D topology of the Fermi surfaces is generally expected in the electron-overdoped compounds. It is noticed that the hole-doped $\text{Ba}_{1-x}\text{K}_x\text{Fe}_2\text{As}_2$ system shows a clearly increasing anisotropy of H_{c2} in overdoped samples²⁵ with a sign change of the superconducting order parameter across different Fermi-surface pockets²⁶, where a Lifshitz transition occurs changing the Fermi-surface topology²⁷. While these results are inspiring, electric-transport measurements were only performed in static fields up to 9 T and, thus, are unlikely to allow a conclusive determination on the nature of H_{c2} and γ throughout the phase diagram.

Here, we report a systematic study of H_{c2} and its anisotropy in electron-doped $\text{BaFe}_{2-x}\text{Ni}_x\text{As}_2$ single crystals at high magnetic fields up to 60 T and low temperatures down to 0.6 K. We establish the doping and temperature dependence both for H_{c2} and γ throughout the superconducting dome with $0.065 \leq x \leq 0.22$. While our data for optimally doped samples are consistent with earlier results⁶⁻⁹, showing a nearly isotropic superconductivity with $\gamma(0) = 1.02$ for the zero-temperature limit, we find that the anisotropy has a very asymmetric doping dependence and increases beyond 2 in the overdoped regime. Further analysis of $H_{c2}(T)$ suggests that the

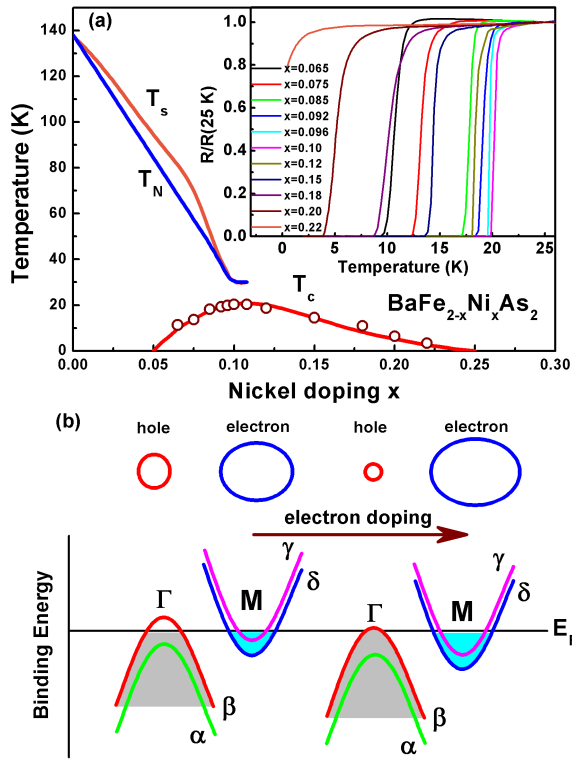


FIG. 1: (color online) (a) Phase diagram of $\text{BaFe}_{2-x}\text{Ni}_x\text{As}_2$, where T_s , T_N , and T_c are the structural, AFM, and superconducting transition temperatures, respectively. The open symbols mark the 12 doping levels studied in this work. The inset shows the sharp superconducting transition of the in-plane resistance normalized at 25 K. (b) Schematic picture of the electron-doping effects on the Fermi pockets and band structure based on a rigid-band model.

anisotropy is intimately related to the change of the Fermi-surface topology together with impurity scattering from the Ni dopants.

II. EXPERIMENT

Electron doped $\text{BaFe}_{2-x}\text{Ni}_x\text{As}_2$ single crystals were grown by the FeAs self-flux method²⁸. Twelve different compositions across the superconducting dome were investigated with nominal Ni contents of $x = 0.065, 0.075, 0.085, 0.092, 0.096, 0.1, 0.108, 0.12, 0.15, 0.18, 0.20, \text{ and } 0.22$, as marked in Fig. 1(a). Note that the real Ni concentration is about 0.8 times the nominal content x ²⁸. All samples show a very narrow superconducting transition width $\Delta T_c \equiv T_c(90\%) - T_c(10\%) < 1$ K [inset of Fig. 1(a)], indicating a high crystal quality. Detailed characterization of these crystals can be found in our previous publications^{18,28}.

The resistivity in the ab plane (ρ_{ab}) was measured by a standard four-probe method with magnetic fields applied parallel to the ab plane ($H \parallel ab$) and the c axis ($H \parallel c$), respectively. The field-dependent magnetoresistivity ρ_{ab} was measured at different temperatures using a 65 T non-destructive pulsed magnet driven by a capacitor bank at the Dresden High

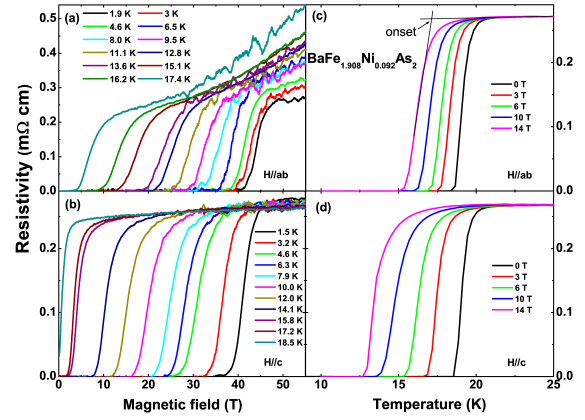


FIG. 2: (color online) (a)-(b) Magnetic-field and (c)-(d) temperature dependence of the in-plane resistivity ρ_{ab} with $H \parallel ab$ and $H \parallel c$ of $\text{BaFe}_{1.908}\text{Ni}_{0.092}\text{As}_2$ measured under pulsed magnetic field and static field in PPMS, respectively. The upper critical field H_{c2} is defined as the onset of the superconducting transitions shown in panel (c).

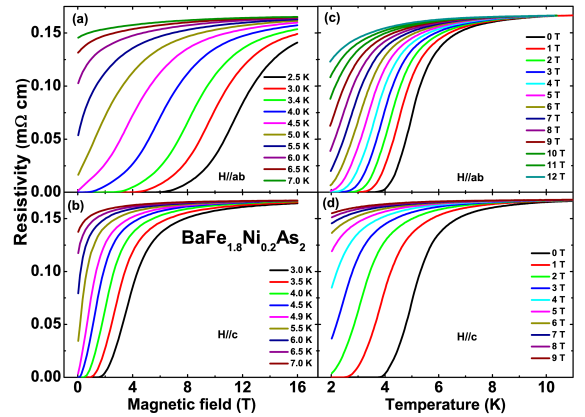


FIG. 3: (color online) (a) - (d) Magnetic-field and temperature dependence of ρ_{ab} with $H \parallel ab$ and $H \parallel c$ in $\text{BaFe}_{1.8}\text{Ni}_{0.2}\text{As}_2$ measured in a 16 T-PPMS.

Magnetic Field Laboratory, with a pulse duration of about 180 ms²⁹. The applied current was 1 mA at a frequency of 30-40 kHz. The voltage was recorded by a digital oscilloscope, Yokogawa DL750, with a high sampling rate of 1 MS/s and a resolution of 16 bit. After the pulse, the signal processing is performed by use of a lock-in software procedure. The down-sweep branch of the pulse was used to determine H_{c2} utilizing its long decay time (about 150 ms). In order to determine the field dependence of H_{c2} near T_c more accurately, the temperature dependence of ρ_{ab} was measured by use of a *Quantum Design* Physical Property Measurement System with magnetic fields up to 14 T (14 T-PPMS). Additional data on the $x = 0.20$ and 0.22 compounds were measured in a 16 T-PPMS down to 2 K and in pulsed magnetic fields in a He-3 bath cryostat down to 0.6 K. To ensure a low noise during the measurements, all Ohmic contacts, made by silver epoxy, had a low resistance of less than 1 Ω .

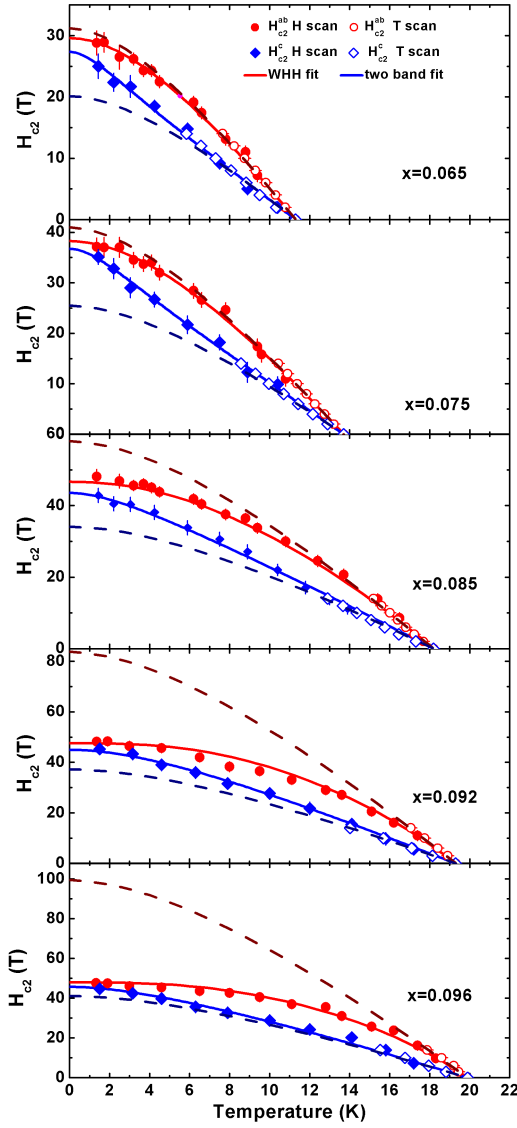


FIG. 4: (color online) Temperature dependence of H_{c2} of the five underdoped samples extracted from the magnetotransport measurements. The solid symbols are obtained from pulse-field measurements by scanning field (H scan), and the open symbols are obtained from PPMS measurements by scanning temperature (T scan). The red solid line shows a WHH fit with the parameters α and λ_{so} given in Table I for H_{c2}^{ab} . The blue solid line is a two-band fit for H_{c2}^c with the parameters D_1 and η given in Table I. The dashed lines are the WHH predictions with $\alpha = 0$ and $\lambda_{so} = 0$ both for H_{c2}^{ab} and H_{c2}^c .

III. RESULTS AND ANALYSIS

We first present typical raw magnetotransport data for the underdoped sample $\text{BaFe}_{1.908}\text{Ni}_{0.092}\text{As}_2$ with $T_c = 19.3$ K and the overdoped sample $\text{BaFe}_{1.8}\text{Ni}_{0.2}\text{As}_2$ with $T_c = 6.4$ K in pulsed and static magnetic fields, as shown in Figs. 2 and 3, respectively. For other dopings, the magnetoresistance data are very similar. Thus, we only show the extracted H_{c2} data in the following.

In Fig. 2, only negligible field-induced broadening of

the resistive transitions is observed, in contrast to what has been observed for $\text{NdFeAsO}_{0.7}\text{F}_{0.3}$ ³, $\text{SmFeAsO}_{0.85}$, and $\text{SmFeAsO}_{0.8}\text{F}_{0.2}$ ⁴, suggesting a very narrow vortex-liquid region in the Ba-122 system. Thus, we determine H_{c2} as the onset of the transition, most closely corresponding to the resistive upper critical field³⁰ [see arrow in Fig. 2(c)]. The full recovery of the normal-state resistivity allows us to determine H_{c2} quantitatively for both field geometries. Apparently, a stronger in-plane field ($H \parallel ab$) is needed to suppress superconductivity, consistent with previous results for iron-based superconductors³⁻¹¹. By carefully comparing the results in Fig. 2 and Fig. 3, one may immediately find that the upper critical field for $H \parallel ab$ (H_{c2}^{ab}) is close to the $H \parallel c$ case (H_{c2}^c) in the underdoped, $x = 0.092$, sample at low temperatures, while a clear difference between H_{c2}^{ab} and H_{c2}^c exists for the overdoped, $x = 0.20$, sample. Therefore, the anisotropy $\gamma = H_{c2}^{ab}/H_{c2}^c$, is electron-doping dependent.

The temperature dependence of H_{c2}^{ab} and H_{c2}^c of the five underdoped samples with $x = 0.065, 0.075, 0.085, 0.092$, and 0.096 , is shown in Fig. 4. The solid symbols are obtained from pulsed-field measurements utilizing magnetic field scans (H scan), and the open symbols are obtained from PPMS measurements by use of temperature scans (T scan). The consistency of the data from two different measurements proves the reliability of the results. For all five samples, $H_{c2}^{ab}(T)$ has a tendency to saturate with decreasing temperature, while $H_{c2}^c(T)$ shows a quasilinear increase and no clear saturation at low temperatures. No obvious upturn of $H_{c2}(T)$ is found for both field directions, with a nearly isotropic H_{c2} at 1.5 K. As the doping level becomes higher, H_{c2} at low temperatures becomes more isotropic.

In general, by applying a magnetic field on a type-II superconductor, the Cooper pairs break up via two independent mechanisms: either by orbital or by spin-paramagnetic effects. The former is associated with screening currents around vortex cores in order to expel the external field and to reduce the condensation energy, while the latter originates from the Zeeman effect. For a single-band superconductor in the dirty limit³², the orbital limit is given by $H_{c2}^{orb}(0) = -0.69dH_{c2}/dT|_{T=T_c}T_c$. Alternatively, the Pauli-limiting field for a weakly coupled BCS superconductor in the absence of spin-orbit scattering can be estimated as³³ $H_p^{BCS}(0)/T_c = 1.86$ T/K. For the typical underdoped sample $\text{BaFe}_{1.908}\text{Ni}_{0.092}\text{As}_2$ (Fig. 2) for example: we obtain $-dH_{c2}^{ab}/dT|_{T_c} = 6.25$ K/T and $-dH_{c2}^c/dT|_{T_c} = 2.78$ K/T, yielding $H_{c2}^{orb,ab}(0) = 83$ T for $H \parallel ab$, $H_{c2}^{orb,c}(0) = 37$ T for $H \parallel c$, and $H_p^{BCS}(0) = 36$ T. These estimates do not agree with our experimental data. To fully describe our results, one must take into account both orbital pair-breaking and spin-paramagnetic effects. Therefore, we use the full Werthamer-Helfand-Hohenberg (WHH) formula that incorporates the spin paramagnetic effect via the Maki parameter α and the spin-orbit scattering constant λ_{so} to describe the experimental H_{c2} data³⁴:

$$\ln \frac{1}{t} = \sum_{\nu=-\infty}^{\infty} \left\{ \frac{1}{|2\nu+1|} - [2\nu+1] + \frac{\bar{h}}{t} + \frac{(\alpha\bar{h}/t)^2}{|2\nu+1| + (\bar{h} + \lambda_{so})/t} \right\}^{-1}, \quad (1)$$

where $t = T/T_c$ and $\bar{h} = (4/\pi^2)[H_{c2}(T)]/[dH_{c2}/dT|_{T_c}]$. As

TABLE I: Summary of the parameters for the upper critical field for all investigated compositions of $\text{BaFe}_{2-x}\text{Ni}_x\text{As}_2$.

x	T_c (K)	$-dH_{c_2}^{ab}/dT _{T_c}$ (T/K)	$-dH_{c_2}^c/dT _{T_c}$ (T/K)	$H_{c_2}^{orb,ab}(0)$ (T)	$H_{c_2}^{orb,c}(0)$ (T)	$H_P^{BCS}(0)$ (T)	α	λ_{so}	D_1	η (D_2/D_1)	$H_{c_2}^{ab}(0)$ (T)	$H_{c_2}^c(0)$ (T)	$\gamma(0)$
0.065	11.3	3.98	2.57	31.0	20.0	20.8	0.33	0	4.10	0.27	29.6	27.3	1.08
0.075	13.7	4.31	2.68	40.7	25.3	25.2	0.38	0	3.70	0.27	38.3	36.7	1.04
0.085	18.2	4.59	2.70	57.6	33.9	33.5	0.70	0.05	3.45	0.38	46.6	43.5	1.07
0.092	19.3	6.25	2.78	83.2	37.0	35.5	1.69	0.12	3.15	0.48	47.6	44.9	1.06
0.096	19.9	7.20	2.98	98.9	40.9	36.6	2.58	0.18	3.10	0.53	48.0	45.7	1.05
0.10	20.3	7.69	3.17	107.7	44.4	38.1	2.77	0.28	3.00	0.55	48.2	47.5	1.02
0.108	20.3	8.42	3.23	117.9	45.2	38.1	3.09	0.33	2.95	0.57	50.0	47.6	1.05
0.12	18.6	7.77	2.98	99.7	38.2	34.2	2.62	0.40	2.88	0.65	49.4	42.6	1.16
0.15	14.5	5.20	2.24	52.7	22.7	26.7	1.20	0.06	2.88	2.00	35.1	25.6	1.37
0.18	10.9	4.36	2.04	32.8	15.3	20.1	0.68	0.04	2.92	3.20	27.6	17.8	1.55
0.20	6.4	4.35	1.50	19.2	6.5	11.8	0	0	3.15	5.50	19.3	9.2	2.09
0.22	3.4	4.25	1.11	10.0	2.6	6.3	0	0	3.90	3.50	10.1	4.2	2.43

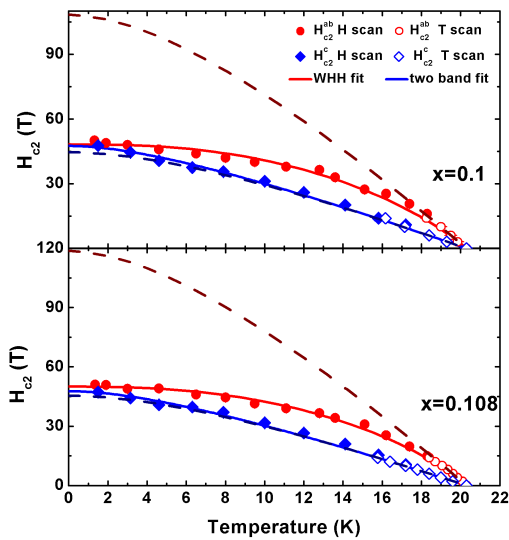


FIG. 5: (color online) Temperature dependence of H_{c_2} of the two samples at optimum doping extracted from the magnetotransport measurements. The solid symbols are obtained from pulse-field measurements, and the open symbols are obtained from PPMS measurements. The red solid line shows a WHH fit with the parameter α and λ_{so} as given in Table I for $H_{c_2}^{ab}$. The blue solid line is a two-band fit for $H_{c_2}^c$ with the parameter D_1 and η given in Table I. The dashed lines are the WHH predictions with $\alpha = 0$ and $\lambda_{so} = 0$ both for $H_{c_2}^{ab}$ and $H_{c_2}^c$.

shown by the red solid line in Fig. 4, the best fit can reproduce the experimental $H_{c_2}^{ab}$ of all the five samples very well. All of the fit parameters we used are listed in Table I for all samples. For $x = 0.092$, we obtain $\alpha = 1.69$ and $\lambda_{so} = 0.12$. The Maki parameter α , defined as $\alpha = \sqrt{2}H_{c_2}^{orb}(0)/H_P(0)$, is comparable to the cases of LiFeAs ^{10,11,35}, KFe_2As_2 ³⁶, and $\text{Ba}_{0.6}\text{K}_{0.4}\text{Fe}_2\text{As}_2$ ⁷, indicating a dominant spin-paramagnetic effect in the upper critical field for $H \parallel ab$. In Fig. 4, one can see that the WHH fit (dashed lines) underestimates the low-temperature data of $H_{c_2}^c(T)$, even when considering the orbital

pair breaking only ($\alpha = \lambda_{so} = 0$), while a similar fit heavily overestimates $H_{c_2}^{ab}(T)$ especially for $x = 0.092$ and 0.096 . Thus, the single-band model cannot fully describe $H_{c_2}^c(T)$ in the underdoped regime.

On the other hand, the quasilinear temperature dependence of $H_{c_2}^c$, which has been commonly observed in MgB_2 and other iron pnictides³⁻⁵, can be understood by an effective two-band model³⁷,

$$a_0[\ln t + U(h)][\ln t + U(\eta h)] + a_1[\ln t + U(h)] + a_2[\ln t + U(\eta h)] = 0. \quad (2)$$

The coefficients a_0 , a_1 , and a_2 , are determined from the BCS coupling tensor $\lambda_{mm'}$ ³⁷. The function $U(x) = \psi(1/2 + x) - \psi(1/2)$, where ψ is the di-gamma function. Other parameters are defined by $h = H_{c_2}D_1/2\phi_0T$ and $\eta = D_2/D_1$, where ϕ_0 is the flux quantum and D_n is the electron diffusivity for the n th Fermi-surface sheet. Here, we assume $a_0 = 1$, $a_1 = 1.5$, and $a_2 = 0.5$ with dominant intraband coupling. Since the line shape mostly depends on the choice of D_1 and η rather than the coupling constants $\lambda_{mm'}$, we only tune D_1 and η to fit $H_{c_2}^c(T)$, where $\eta \neq 1$ means different intraband scattering on each Fermi sheet. The two-band fits agree very well with the $H_{c_2}^c(T)$ data (blue solid lines in Fig. 4). We have also tried to fit $H_{c_2}^{ab}(T)$ with a two-band fit, but this does not capture the saturation of $H_{c_2}^{ab}(T)$ due to strong paramagnetic effect. Therefore, we used a single-band WHH fit for $H_{c_2}^{ab}(T)$ and two-band fit for $H_{c_2}^c(T)$ separately, as shown by solid lines in Fig. 4. The best fit parameters are listed in Table I.

We have as well analyzed the data for the optimally doped and overdoped samples in the same way. The fit results are shown in Figs. 5 and 6 with the parameters given in Table I. For the samples at optimum doping (Fig. 5), the single-band WHH fit considering the orbital pair breaking only ($\alpha = \lambda_{so} = 0$) overestimates $H_{c_2}^c(T)$ heavily as for the underdoped sample, and underestimates the low-temperature data of $H_{c_2}^c(T)$ slightly. Although a two-band model can better describe the data, the two-band effect may be weaker than for the underdoped sample. Interestingly, $H_{c_2}(T)$ at low temperatures becomes very isotropic with $\gamma(0) = 1.02$ for $x = 0.10$, which is

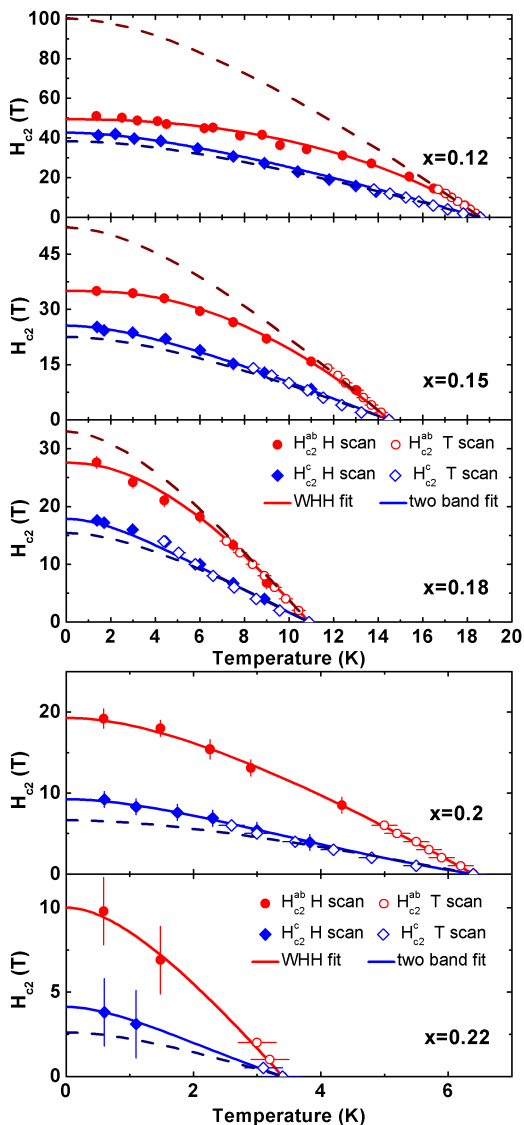


FIG. 6: (color online) Temperature dependence of H_{c2} of the five overdoped samples extracted from the magnetotransport measurements. The solid symbols are obtained from pulse-field measurements, and the open symbols are obtained from PPMS measurements. The red solid line shows a WHH fit H_{c2}^{ab} . The blue solid line is a two-band fit for H_{c2}^c . The fit parameters are given in Table I. The dashed lines are the WHH predictions with $\alpha = 0$ and $\lambda_{so} = 0$ both for H_{c2}^{ab} and H_{c2}^c .

the smallest anisotropy among all measured iron-based superconductors until now³⁻¹⁰.

The overdoped samples show opposite behavior compared to the underdoped samples. As shown in Fig. 6, by increasing Ni doping from $x = 0.12$ to $x = 0.22$, the anisotropy of H_{c2} at low temperature grows quickly, and the pure orbital WHH fits (dashed lines) clearly deviate from the $H_{c2}^c(T)$ data but agree well with the $H_{c2}^{ab}(T)$ data. Especially for the heavily overdoped sample with $x = 0.22$, the spin-paramagnetic effects are negligible due to the absent saturation of $H_{c2}^{ab}(T)$. However, we still need the two-band model to describe $H_{c2}^c(T)$

in the overdoped regime. Although the electronic diffusivity D_1 slightly varies between 3 and 4, the diffusivity ratio $\eta = D_2/D_1$ rapidly grows from 0.27 to 5.5 upon electron doping. The large increase of the diffusivity ratio $\eta = D_2/D_1$ suggests enhanced electronic mobility for one of the bands or a significant change of the relative scattering rate for each band upon electron doping. By approaching zero temperature, the anisotropy is beyond 2 for $x = 0.20$ and $x = 0.22$, clearly different from the nearly isotropic superconductivity for the underdoped and optimally doped samples.

IV. DISCUSSION

By fitting the $H_{c2}(T)$ data in Fig. 4 - Fig. 6 (solid lines), we obtain the upper critical field $H_{c2}(0)$ for the zero-temperature limit with $\sim 5\%$ accuracy. We finally summarize the doping dependence of $H_{c2}(0)$ and their anisotropy $\gamma(0)$ in Fig. 7 for the whole superconducting dome from $x = 0.065$ to 0.22. The gradient color in Fig. 7 maps the temperature dependence of the anisotropy γ for all samples, where all of them show an increasing anisotropy upon warming to T_c . The overall doping-dependent features of $H_{c2}^{ab}(0)$ and $H_{c2}^c(0)$ follow the superconducting dome, while their difference quickly increases especially on the overdoped side, resulting in an abrupt increase of $\gamma(0)$ when $x > 0.1$. As shown in the inset of Fig. 7, the overall doping dependence of $\gamma(0)$ is highly asymmetric with a minimum $\gamma(0) = 1.02$ at optimal doping $x = 0.10$, which should be related to the asymmetric superconducting dome in the $\text{BaFe}_{2-x}\text{Ni}_x\text{As}_2$ system.

It is argued, that the nearly isotropic H_{c2} for most of the optimally doped iron pnictides may originate either from Pauli-limiting or band-warping effects along the k_z direction^{7,10,20,23,38}. In our results, the Pauli-limiting effect (marked as α) is indeed strongest around optimum doping, then quickly weakens, and finally vanishes in the overdoped samples, resulting in small $H_{c2}^{ab}(0)$ and $\gamma(0)$ for optimally doped compounds, and larger $H_{c2}^{ab}(0)$ and $\gamma(0)$ for the overdoped samples. However, this simple picture cannot explain the difference in γ between the underdoped ($x = 0.085$) and the overdoped ($x = 0.18$) samples with similar values of α and λ_{so} (Table I). On the other hand, upon doping electrons, the warped cylindrical Fermi surface around the Γ -Z line first transforms to a 3D ellipsoid centered at the Z point, and completely disappears near the concentration where superconductivity appears, while the electron Fermi-surface sheet around the X point continuously increases^{23,24}. We also notice that the two-band fits of $H_{c2}^c(T)$ show a crossover of the diffusivity ratio $\eta = D_2/D_1$ from $\eta < 1$ to $\eta > 1$ around $x \approx 0.12$, corresponding to the disappearance of the hole pocket at the Γ point. Thus, the Ni dopants remarkably affect the scattering rate and induce an unbalanced mobility between the electron and hole band and additionally change the topology of the Fermi surface. Indeed, recent calculations suggest that the Co/Ni dopants in 122 compounds increase the impurity potential and introduce stronger scattering on the hole band accompanied by a weak interband scattering^{21,39,40}.

Therefore, the doping-dependent anisotropy of the super-

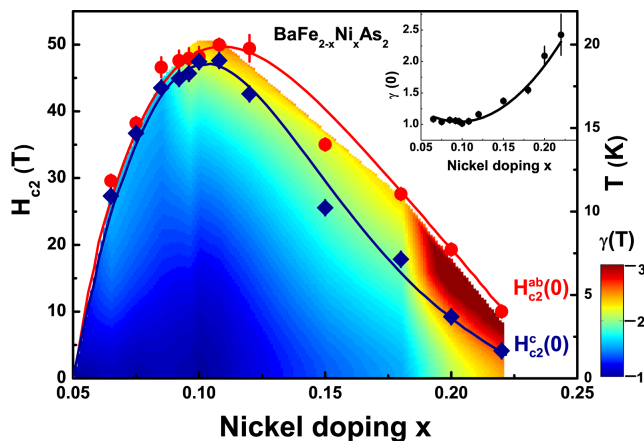


FIG. 7: (color online) Doping dependence of H_{c2}^{ab} , H_{c2}^c , and γ at 0 K. The gradient color maps the temperature dependence of the anisotropy γ (right axis).

conductivity in $\text{BaFe}_{2-x}\text{Ni}_x\text{As}_2$ can be understood by the dual effects from the Fermi-surface topology and impurity scattering. At first, the 3D-like hole Fermi surface with dominant diffusivity tends to form a nearly isotropic superconductivity in the underdoped compounds⁴¹. Then the warping effect of the hole sheets becomes more prominent after doping more electrons, and it tends to form an isotropic superconductivity as well. By further doping Ni into the overdoped regime, the charge carriers from the tiny hole pocket around the Z point are mostly localized and contribute insignificantly to the superconductivity. While the less-warped electron Fermi surface with large volume and high mobility gives rise to a deviation

from isotropic superconductivity, leading to a highly asymmetric doping dependence of $\gamma(0)$ significantly enhanced in the overdoped regime. Thus, the optimum doping with the most isotropic superconductivity, correlates with an isotropic scattering from different Fermi surfaces with fine-tuned scattering rate and Fermi-surface topology.

V. SUMMARY

In summary, we have investigated the temperature dependence of the upper critical field (H_{c2}) in a series of $\text{BaFe}_{2-x}\text{Ni}_x\text{As}_2$ ($0.065 \leq x \leq 0.22$) single crystals in magnetic fields up to 60 T aligned both within the ab plane and along the c axis. All $H_{c2}^{ab}(T)$ data can be fitted by the WHH formula including orbital and spin-paramagnetic effects, while the quasi-linear $H_{c2}^c(T)$ data can be described by an effective two-band model. The anisotropy of H_{c2} at 0 K, $\gamma(0)$, is close to 1 for the underdoped and optimally doped samples, but increases beyond 2 for the overdoped samples, forming a highly asymmetric doping dependence similar to the superconducting dome. Our results indicate that the superconducting anisotropy is determined by the topology of the Fermi surfaces together with the doping-induced impurity scattering, and that the multi-band physics is important for the optimal superconductivity in iron pnictides.

We acknowledge the support of the HLD at HZDR, member of the European Magnetic Field Laboratory (EMFL). The work at IOP, CAS, is supported by MOST (973 project: 2011CBA00110 and 2012CB821400), NSFC (11374011 and 11374346), and CAS (SPRP-B: XDB07020300).

* Electronic address: z.wang@hzdr.de

† Electronic address: hqluo@iphy.ac.cn

¹ Y. Kamihara, T. Watanabe, M. Hirano, and H. Hosono, J. Am. Chem. Soc. **130**, 3296-3297 (2008).

² Z. S. Wang, H. Q. Luo, C. Ren, and H. H. Wen, Phys. Rev. B **78**, 140501 (2008).

³ J. Jaroszynski, F. Hunte, L. Balicas, Y. -j. Jo, I. Raičević, A. Gurevich, D.C. Larbalestier, F.F. Balakirev, L. Fang, P. Cheng, Y. Jia, and H. -H. Wen, Phys. Rev. B **78**, 174523(2008).

⁴ H. -S. Lee, M. Bartkowiak, J. -H. Park, J. -Y. Lee, J. -Y. Kim, N. -H. Sung, B.K. Cho, C.-U. Jung, J.S. Kim, and H. -J. Lee, Phys. Rev. B **80**, 144512 (2009).

⁵ F. Hunte, J. Jaroszynski, A. Gurevich, D. . Larbalestier, R. Jin, A.S. Sefat, M. A. McGuire, B. C. Sales, D. K. Christen, and D. Mandrus, Nature **453**, 903 (2008).

⁶ M. M. Altarawneh, K. Collar, C. H. Mielke, N. Ni, S. L. Budko, and P. C. Canfield, Phys. Rev. B **78**, 220505 (2008).

⁷ H. Yuan, J. Singleton, F. F. Balakirev, S. A. Baily, G. Chen, J. Luo, and N. Wang, Nature **457**, 565 (2009).

⁸ M. Kano, Y. Kohama, D. Graf, F. Balakirev, A. S. Sefat, M. A. McGuire, B. C. Sales, D. Mandrus, and S. W. Tozer, J. Phys. Soc. Jpn. **78**, 084719 (2009).

⁹ S. Khim, J. W. Kim, E. S. Choi, Y. Bang, M. Nohara, H. Takagi, and K.H. Kim, Phys. Rev. B **81**, 184511 (2010).

¹⁰ S. Khim, B. Lee, J. W. Kim, E. S. Choi, G. R. Stewart, and K. H. Kim, Phys. Rev. B **84**, 104502 (2011).

¹¹ J. L. Zhang, L. Jiao, F. F. Balakirev, X. C. Wang, C. Q. Jin, and H. Q. Yuan, Phys. Rev. B **83**, 174506 (2011).

¹² M. Rotter, M. Tegel, D. Johrendt, I. Schellenberg, W. Hermes, and R. Pöttgen, Phys. Rev. B **78**, 020503(R) (2008).

¹³ M. Rotter, M. Tegel, and D. Johrendt, Phys. Rev. Lett. **101**, 107006 (2008).

¹⁴ L. J. Li, Y. K. Luo, Q. B. Wang, H. Chen, Z. Ren, Q. Tao, Y. K. Li, X. Lin, M. He, Z. W. Zhu, G. H. Cao, and Z. -A. Xu, New J. Phys. **11** 025008 (2009).

¹⁵ N. Ni, A. Thaler, J. Q. Yan, A. Kracher, E. Colombier, S. L. Bud'ko, P. C. Canfield, and S. T. Hannahs, Phys. Rev. B **82**, 024519 (2010).

¹⁶ D. Mandrus, A. S. Sefat, M. A. McGuire, and B. C. Sales, Chem. Mater. **22**, 715 (2010).

¹⁷ S. Aswartham, M. Abdel-Hafiez, D. Bombor, M. Kumar, A. U. B. Wolter, C. Hess, D. V. Evtushinsky, V. B. Zabolotnyy, A. A. Kordyuk, T. K. Kim, S. V. Borisenko, G. Behr, B. Büchner, and S. Wurmehl, Phys. Rev. B **85**, 224520 (2012).

¹⁸ H. Luo, R. Zhang, M. Laver, Z. Yamani, M. Wang, X. Lu, M. Wang, Y. Chen, S. Li, S. Chang, J. W. Lynn, and P. Dai, Phys. Rev. Lett. **108**, 247002 (2012).

¹⁹ X. Lu, H. Gretarsson, R. Zhang, X. Liu, H. Luo, W. Tian, M.

- Laver, Z. Yamani, Y. -J. Kim, A. H. Nevidomskyy, Q. Si, and P. Dai, *Phys. Rev. Lett.* **110**, 257001 (2013).
- ²⁰ P. Richard, T. Qian, and H. Ding, arXiv: 1503.07269.
- ²¹ T. Berlijn, C. -H. Lin, W. Garber, and W. Ku, *Phys. Rev. Lett.* **108**, 207003 (2012).
- ²² S. Blackburn, B. Prévost, M. Bartkowiak, O. Ignatchik, A. Polyakov, T. Förster, M. Côté, G. Seyfarth, C. Capan, Z. Fisk, R. G. Goodrich, I. Sheikin, H. Rosner, A. D. Bianchi, and J. Wosnitzer, *Phys. Rev. B* **89**, 220505(R) (2014).
- ²³ S. Ideta, T. Yoshida, I. Nishi, A. Fujimori, Y. Kotani, K. Ono, Y. Nakashima, S. Yamaichi, T. Sasagawa, M. Nakajima, K. Kihou, Y. Tomioka, C. H. Lee, A. Iyo, H. Eisaki, T. Ito, S. Uchida, and R. Arita, *Phys. Rev. Lett.* **110**, 107007 (2013).
- ²⁴ C. Liu, A. D. Palczewski, R. S. Dhaka, T. Kondo, R. M. Fernandes, E. D. Mun, H. Hodovanets, A. N. Thaler, J. Schmalian, S. L. Bud'ko, P. C. Canfield, and A. Kaminski, *Phys. Rev. B* **84**, 020509(R) (2011).
- ²⁵ Y. Liu, M. A. Tanatar, W. E. Straszheim, B. Jensen, K. W. Dennis, R. W. McCallum, V. G. Kogan, R. Prozorov, and T. A. Lograsso, *Phys. Rev. B* **89**, 134504 (2014).
- ²⁶ S. Zhang, Y. P. Singh, X. Y. Huang, X. J. Chen, M. Dzero, C. C. Almasan, arXiv:1507.03628.
- ²⁷ S.N. Khan and D.D. Johnson, *Phys. Rev. Lett.* **112**, 156401 (2014).
- ²⁸ Y. Chen, X. Lu, M. Wang, H. Luo, and S. Li, *Supercond. Sci. Technol.* **24**, 065004 (2011).
- ²⁹ S. Zherlitsyn, T. Herrmannsdoerfer, Yu. Skourski, A. Sytcheva, and J. Wosnitzer, *J. Low Temp. Phys.* **146**, 719 (2007).
- ³⁰ S. I. Vedenev, B. A. Piot, D. K. Maude, and A. V. Sadakov, *Phys. Rev. B* **87**, 134512 (2013).
- ³¹ R. I. Rey, C. Carballeira, J. Mosqueira, S. Salem-Sugui Jr, A. D. Alvarenga, H. Luo, X. Lu, Y. Chen and F. Vidal, *Supercond. Sci. Technol.* **26**, 055004 (2013).
- ³² E. Helfand and N. R. Werthamer, *Phys. Rev.* **147**, 288 (1966).
- ³³ A. M. Clogston, *Phys. Rev. Lett.* **9**, 266 (1962).
- ³⁴ N. Werthamer, E. Helfand, and P. Hohenberg, *Phys. Rev.* **147**, 295 (1966).
- ³⁵ K. Cho, H. Kim, M.A. Tanatar, Y. J. Song, Y. S. Kwon, W.A. Coniglio, C. C. Agosta, A. Gurevich, and R. Prozorov, *Phys. Rev. B* **83**, 060502 (2011).
- ³⁶ T. Terashima, M. Kimata, H. Satsukawa, A. Harada, K. Hazama, S. Uji, H. Harima, G. Chen, J. Luo, and N. Wang, *J. Phys. Soc. Jpn.* **78**, 063702 (2009).
- ³⁷ A. Gurevich, *Phys. Rev. B* **67**, 184515 (2003).
- ³⁸ S. A. Baily, Y. Kohama, H. Hiramatsu, B. Maiorov, F. F. Balakirev, M. Hirano, and H. Hosono, *Phys. Rev. Lett.* **102**, 117004 (2009).
- ³⁹ S. Ishida, M. Nakajima, T. Liang, K. Kihou, C. H. Lee, A. Iyo, H. Eisaki, T. Kakeshita, Y. Tomioka, T. Ito, and S. Uchida, *Phys. Rev. Lett.* **110**, 207001 (2013).
- ⁴⁰ A. S. Sefat, R. Jin, M. A. McGuire, B. C. Sales, D. J. Singh, and D. Mandrus, *Phys. Rev. Lett.* **101**, 117004 (2008).
- ⁴¹ G. T. Wang, Y. Qian, G. Xu, X. Dai, and Z. Fang, *Phys. Rev. Lett.* **104**, 047002 (2010).